Atomistic study of two-level systems in amorphous silica

T. Damart and D. Rodney
Institut Lumière Matière, UMR 5306 Université Lyon 1-CNRS, Université de Lyon, F-69622 Villeurbanne, France

(Received 5 October 2017; published 8 January 2018)

Internal friction is analyzed in an atomic-scale model of amorphous silica. The potential energy landscape of more than 100 glasses is explored to identify a sample of about 700 two-level systems (TLSs). We discuss the properties of TLSs, particularly their energy asymmetry and barrier as well as their deformation potential, computed as longitudinal and transverse averages of the full deformation potential tensors. The discrete sampling is used to predict dissipation in the classical regime. Comparison with experimental data shows a better agreement with poorly relaxed thin films than well relaxed vitreous silica, as expected from the large quench rates used to produce numerical glasses. The TLSs are categorized in three types that are shown to affect dissipation in different temperature ranges. The sampling is also used to discuss critically the usual approximations employed in the literature to represent the statistical properties of TLSs.

DOI: 10.1103/PhysRevB.97.014201

I. INTRODUCTION

Internal friction is responsible for the limited quality factor of glass-based devices, such as electromechanical systems [1–3] or the mirror coatings of gravitational wave detectors [4–6]. In crystals, defects such as impurities [7] and dislocations [8] are known to be the main sources of mechanical dissipation but in disordered solids, the origin of dissipation remains largely elusive, in part because of the strong disparities in short- and medium-range orders among glasses.

It is well accepted that in oxide glasses, such as silica, mechanical waves of low frequencies [hertz (Hz) to megahertz (MHz)] are attenuated because of their interactions with thermally-activated relaxations (TARs) when the temperature is above a few Kelvin. The resulting dissipation is understood in the framework of the two-level system (TLS) model [9–12] where the complexity of the potential energy landscape (PEL) of the glass is represented by a distribution of double-well potentials corresponding to pairs of local potential energy minima. The dynamics in the double-well potentials is controlled at very low temperatures by quantum tunneling but hopping between minima becomes thermally-activated at higher temperatures [13,14]. When a mechanical wave passes through the glass, the solid is deformed and so is the PEL, bringing the TLSs out of equilibrium. The TLSs return to equilibrium with a thermally activated relaxation time, which may come into resonance with the frequency of the forcing wave, thus producing dissipation.

There have been numerous studies on glasses and more specifically in amorphous silica (SiO_2) to quantify energy dissipation and unravel its atomic origin. These studies were carried out through internal friction measurements in resonators, such as vibrating spheres or beams [15–21], attenuation measurements of acoustic waves [22], Brillouin-scattering [23–25], and more recently atomic-scale simulations [26–28]. The amorphous silica samples used in these works are of three kinds: well-relaxed vitreous bulk silica obtained through the slow heating and cooling of crystalline SiO_2, poorly relaxed thin films deposited using ion beam sputtering (IBS), and numerical silica produced by molecular dynamics (MD). Dissipation (Q^{-1}) measured experimentally at low frequencies shows a plateau at low temperature (<5 K) in the quantum tunneling regime, followed by a maximum of dissipation, $Q^{-1} \approx 10^{-3}$, at around 30 to 50 K [17]. In the case of vitreous silica, this maximum is followed by a drop of four orders of magnitude reaching $Q^{-1} \approx 10^{-7}$ at 300 K [17–19,25], while for IBS silica, the dissipation decreases slowly to $Q^{-1} \approx 10^{-4}$ before presenting two smaller maxima at 150 and 250 K [21], recently reproduced by numerical simulations [28].

The TLS model has been used successfully to fit experimental data in vitreous bulk silica, see, for instance, Refs. [18,23,24,29–31]. However, this top-bottom approach suffers from two limitations: (1) the experimental measurements yield spatially averaged properties and cannot probe individual TLSs; (2) simplifying assumptions had to be used to represent the statistical properties of the TLSs in order to make the fit technically feasible. In particular, the energy asymmetry between the TLS states and the energy barrier were assumed statistically independent and given by predefined distributions. A bottom-up approach starting at the atomistic scale has also been attempted, identifying TLSs in model Lennard-Jones glasses [32] and in more realistic models of oxide glasses, silica [26–28], and tantalum oxide [33]. These data were used as input of a TLS model to predict dissipation, but simplifying approximations were still used.

In the present paper, we build on this bottom-up approach to predict dissipation using the TLS model based on an atomic-scale exploration of the PEL of amorphous silica. In contrast with previous studies, we make no assumption on the statistical properties of the TLSs and use a discrete sample to compute dissipation. Moreover, analyzing the atomic rearrangements involved in the TLSs, we propose a classification based on three categories, which affect dissipation in different ranges of temperature. The paper is organized as follows. Section II introduces a revised expression of the TLS model accounting for the full tensorial nature of the deformation and the *a priori*

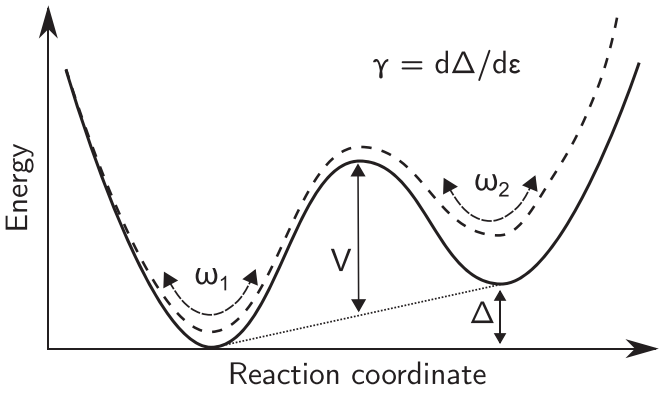

FIG. 1. Schematic representation of a two-level system, with two metastable states connected by a double-well potential. The dashed curve represents the potential under a strain ϵ.

difference in attempt frequencies between the initial and final states of the TLSs. In Sec. III, we discuss the physical and atomic characteristics of the TLSs, which are then used in Sec. IV to predict dissipation numerically.

II. METHODOLOGY

A. Two-level system model

As illustrated in Fig. 1, a TLS can be characterized by the energy asymmetry F1between its initial and final states (noted 1 and 2), $\Delta = E_2 - E_1$, by the average energy barrier, $V = \frac{E_a - E_1}{2} + \frac{E_a - E_2}{2} = E_a - \frac{\Delta}{2}$ (where E_a is the activation energy), the attempt frequencies in the initial and final states $\omega_{1/2}$, and the deformation potential tensor $\bar{\bar{\gamma}} = \partial\Delta/\partial\bar{\bar{\epsilon}}$, which represents the sensitivity of the asymmetry Δ on an applied strain tensor $\bar{\bar{\epsilon}}$.

The dissipation due to TLSs has been expressed in seminal works [9–14], using the harmonic transition state theory (hTST) [34] in the linear regime and assuming independent TLSs. We revisit this derivation in Appendix A to stress its relation with the eigenstrain approach of defect mechanics [35] and to account explicitly for the difference of attempt frequencies in both states of the TLSs and the tensorial nature of the deformation potential. Dissipation at a frequency ω is expressed as

$$Q^{-1}(\omega) = \frac{1}{\mathcal{V}C} \sum_{\ell,\mathrm{TLS}} A_\ell \frac{\omega\tau_\ell}{1+\omega^2\tau_\ell^2} \gamma_\ell^2 \tag{1}$$

with

$$A_\ell = \frac{1}{4k_BT} \operatorname{sech}^2\left(\frac{\Delta}{2k_BT} + \frac{1}{2}\ln\frac{\omega_{2,\ell}}{\omega_{1,\ell}}\right) \tag{2}$$

and the relaxation time

$$\tau_\ell = \frac{\pi}{\sqrt{\omega_{1,\ell}\omega_{2,\ell}}} \exp\left(\frac{V}{k_BT}\right) \operatorname{sech}\left(\frac{\Delta}{2k_BT} + \frac{1}{2}\ln\frac{\omega_{2,\ell}}{\omega_{1,\ell}}\right), \tag{3}$$

where $\mathcal{V}$ is the sample volume and C the appropriate elastic modulus (longitudinal or transverse). The deformation potential γ_ℓ appears quadratically and must be averaged over all possible orientations of the TLSs with respect to the applied strain. As detailed in Appendixes B and C, this results in two different quadratic averages depending on whether the deformation is longitudinal or transverse [see Eqs. (B2) and (C2)]. The relaxation time depends on an effective attempt frequency, $\sqrt{\omega_1\omega_2}$, which depends on the product of the attempt frequencies in the initial and final configurations that are not assumed equal a priori.

Equation (1) is usually transformed into an integral by replacing the attempt frequencies and deformation potentials by their averages and introducing statistical distributions for Δ and V. By way of contrast, we will keep here the discrete sum over TLSs in Eq. (1) and will evaluate whether dissipation can be predicted without using any statistical approximation.

TABLE I. Average first-neighbor coordination numbers in the present numerical SiO_2 glasses.

Silicium	%	Oxygen	%
Coord. 4	99.7	Coord. 1	0.1
Coord. 5	0.3	Coord. 2	99.7
		Coord. 3	0.2

B. Atomic-scale glass model

To generate representative samples of TLSs, 115 glassy structures of silica were synthesized using molecular dynamics (MD) by quenching a melt from 5000 K down to 0 K at a constant quench rate of 10^{11} K s^{-1}. All samples are cubic and periodic with a size $L = 34.77$ Å. They contain 3000 atoms (1000 silicon and 2000 oxygen atoms) at a density of 2.4 g/cm^3, which corresponds to zero average pressure with the present potential [36]. Atomic interactions are modeled with the standard van Beest-Kramer-van Santen (BKS) pair potential [37], which is known to reproduce accurately the structure [36,38,39] and pressure response of amorphous SiO_2 [40,41]. The calculations are further optimized using a Wolf truncation, with the smoothing function proposed by Carré *et al.* [42] and already employed in Refs. [36,40,43]. As expected, the samples form tetrahedral networks, with a short-range order made of SiO_4 tetrahedra and a medium-range order consisting mainly of five- and six-membered Si-O rings [36,44,45]. Average coordination numbers are shown in Table I, highlighting that the samples contain very few coordination defects, although we will see in the following that they strongly affect low-frequency dissipation.

C. Exploring the potential energy landscape

To find TLSs, we need to explore the potential energy landscape (PEL) around the glassy structures to identify transitions with low-energy barriers. We follow the methodology proposed by Reinisch and Heuer [26] and already used by Hamdan *et al.* [27] in amorphous SiO_2. MD simulations were used at finite temperature to induce transitions and a double-ended transition method was employed to reconstruct the energy barriers. In the present case, we used the nudged elastic band (NEB) method [46,47].

More specifically, for each of the 115 samples, we generated 1000 trajectories at constant temperature (1000 K), starting with different initial random velocities. Every 40 fs (40 time

steps), the energy was minimized, checking whether the system returned to the initial configuration during relaxation. In this case, the MD run was continued until either a new configuration was obtained or the simulated time reached 10 ps. The newly found configurations were compared using a distance criterion of 1.0 Å to eliminate duplicates, i.e., we produced a set of final configurations separated from each other by more than 1.0 Å in configuration space. We then employed a climbing NEB [48] algorithm to find the minimum energy path between the initial and final configurations. The path between the initial and final configurations was discretized in 50 images linked in configuration space by springs with a spring constant of 1.0 eV/Å^2. The initial path was linearly interpolated between initial and final configurations. We used the same maximum force criterion of 2.5×10^{-5} eV/Å for both the energy minimizations and NEB calculations. From the minimum energy paths, the energy asymmetry (Δ) and barrier ($V = E_a - \Delta/2$) were obtained, as illustrated in Fig. 1. We checked that the energy asymmetry depends negligibly on the cell size by taking a few final configurations and building systems three times larger in all three directions by surrounding the configurations with copies of the initial configuration. We then rerelaxed these larger systems and recomputed the energy asymmetry. We found relative variations of Δ below 3%.

Using this technique, energy barriers are searched with a bias due to Boltzmann factor, $\exp(-E_a/k_BT)$. The search temperature has therefore to be chosen carefully, high enough so that the system traverses as many barriers as possible, but not too high to remain in a glassy state. Here, we chose about 80% of the mode-coupling temperature, the reference temperature for the dynamics of liquids at the atomic scale [49]. Even at this high temperature, only low-energy barriers, with activation energies typically below 1 eV are identified. Another advantage of the present method is that the searches follow physical dynamics and probe paths in the PEL along which the system goes naturally. The main disadvantage of this approach is that it is numerically highly inefficient because most searches pass through the same few low-energy barriers that have a high Boltzmann factor, requiring to perform many searches to obtain a sufficient sampling.

D. Deformation potential and attempt frequency

Two more parameters need to be computed to predict dissipation from the TLS model: the deformation potential tensor, $\gamma_{ij} = \partial\Delta/\partial\epsilon_{ij}$, and the attempt frequencies in the initial and final configurations, $\omega_{1/2}$. The deformation potential depends on the eigenstrain generated when the TLS transforms from state 1 to state 2. As shown in Appendix A [Eq. (A10)], the deformation potential can be computed from the difference in internal stresses between both states:

$$\gamma_{ij} = \mathcal{V}\Delta\sigma_{ij}. \tag{4}$$

We checked using finite-difference calculations that this expression is indeed equivalent to the usual definition $\gamma_{ij} = \partial\Delta/\partial\epsilon_{ij}$.

Finally, the attempt frequencies in the initial and final configurations of each TLS were computed using the hTST [34] from the ratio of the real, strictly positive eigenfrequencies in the initial and activated states of each transition:

$$\omega_{1/2} = \frac{\prod_{i=1}^{3N-3}\omega_{1/2,i}}{\prod_{i=1}^{3N-4}\omega_i^\star}. \tag{5}$$

For this, we used an exact diagonalization of the dynamical matrix of the initial, final, and activated configurations of each TLS. The activated configurations have exactly one strictly negative eigenvalue because the NEB method converges to the minimum energy path and the climbing procedure brings the maximum energy image to the saddle configuration [48]. We did not add an entropic correction as done in Refs. [27,28,33] since the latter should emerge from the PEL exploration.

III. TWO-LEVEL SYSTEMS

A. TLS properties

1. TLS density

From the MD searches detailed above, 668 different transitions were identified, which represents 1.93 transitions/1000 atoms or 1.4×10^{-4} TLS/Å^3. This number is, however, not well-defined since it necessarily increases with the search temperature. We also checked that this density increases in less-relaxed glasses by considering systems quenched at 10^{12} K s^{-1}. From the data analyzed by Vacher *et al.* [24], an experimental density of 810^{-5} TLS/Å^3 can be estimated, which is about half the present density. However, we will see below that only a limited fraction of the transitions identified in the numerical glasses contribute to the dissipation, while the experimental density only reflects the contributing TLSs.

2. Energy asymmetry and barrier

Figure 2 shows the TLS energy asymmetry, Δ, as a function of the energy barrier V. As expected from the bias by Boltzmann factor of the MD searches, very few barriers with V larger than 0.5 eV were found. Also, there are no barriers above the $\Delta = 2V$ line, i.e., for all barriers, $\Delta < 2V$. This is a direct consequence of the definition of the energy barrier, $V = E_a - \Delta/2$, and the condition $E_a > \Delta$. This simple observation rules out the common assumption that V and Δ are statistically independent. We also note that very few transitions have a

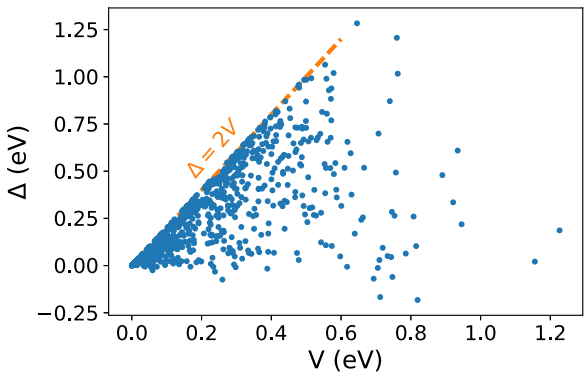

FIG. 2. Asymmetry Δ as a function of the TLS energy barrier V for 668 TLSs. The orange dashed line represents the maximum possible asymmetry $\Delta = 2V$ for a TLS of energy barrier V.

negative asymmetry, an indication that the present glasses are well relaxed.

Finally, we note that there is a rather high density of transitions near the $\Delta = 2V$ line. They correspond to highly asymmetrical transitions, with the saddle state at almost the same energy as the final state. We will see below that these transitions do not contribute to dissipation.

3. Deformation potential

The longitudinal and transverse deformation potentials, γ_L^2 and γ_T^2, respectively, are shown in Fig. 3 as a function of V. Both potentials show similar behavior, as expected from the similarity between Eqs. (B2) and (C2).

Experimentally, values of 1.08 and 0.42 eV^2 were reported by Doussineau *et al.* [50] for the longitudinal and transverse potentials, respectively. Numerical average deformation potentials between 1 and 2 eV were also reported by Hamdan *et al.* [27] and Billman *et al.* [28]. These values are significantly lower than the bulk of the data obtained here. However, the experiments were performed at extremely low temperatures (in the range 0.1 to 1.5 K) and therefore correspond to very low energy barriers crossed with the help of quantum tunneling. We see in Fig. 3 that, indeed, the lowest barriers have low deformation potentials in the experimental range. However, the TLSs with higher barriers, which are relevant for dissipation in the classical regime, have deformation potentials about a hundred times higher.

The ratio between longitudinal and transverse deformation potentials was studied by Heuer [51] as a universal measure of disorder in glasses. Experimental data in the quantum regime over a wide range of glasses [29] show a ratio $\gamma_L^2/\gamma_T^2 = 2.6 \pm 0.4$. The present data, which extend beyond the quantum regime, have interestingly a similar average ratio, of about 2.7. Inspecting Eqs. (B2) and (C2), we see that for a given TLS, γ_L^2/γ_T^2 is a function of I_1^2/I_2 alone, with $I_1 = \mathrm{tr}(\bar{\bar{\gamma}})$ and $I_2 = \mathrm{tr}(\bar{\bar{\gamma}}^2)$, two invariants of the deformation potential tensor:

$$\frac{\gamma_L^2}{\gamma_T^2} = \frac{4}{3}\frac{1+\frac{1}{2}\left(\frac{I_1^2}{I_2}\right)}{1-\frac{1}{3}\left(\frac{I_1^2}{I_2}\right)}, \tag{6}$$

The minimum value of the ratio is 4/3, as noted in Ref. [51], obtained when $I_1 = 0$, i.e., when the eigenstrain of the TLS corresponds to pure shear. The longitudinal deformation potential is therefore necessarily larger than the transverse potential and cannot be zero because shear deformations involve tensile strains. On the other hand, if the eigenstrain is a pure dilatation, $I_1^2 = 3I_2$, the transverse potential vanishes and γ_L^2/γ_T^2 is infinite. This ratio is therefore a measure of the relative weights between the TLS shear and dilatation. Figure 3(c) shows this ratio for each TLS of the sample. The values cover about an order of magnitude, with a higher density at small ratios close to 4/3. TLSs have therefore a marked shear component, but dilatations are also involved.

4. Attempt frequency

The effective attempt frequency, $\sqrt{\omega_1\omega_2}$, which appears in the prefactor of the relaxation time in Eq. (3) is plotted in Fig. 4. The values are rather homogeneously spread, showing no hint of correlation with V. The average frequency, 13.6 THz, is in-between the two experimental values reported in bulk vitreous SiO_2, 10.5 THz [24], and IBS thin films, 18.9 THz [21].

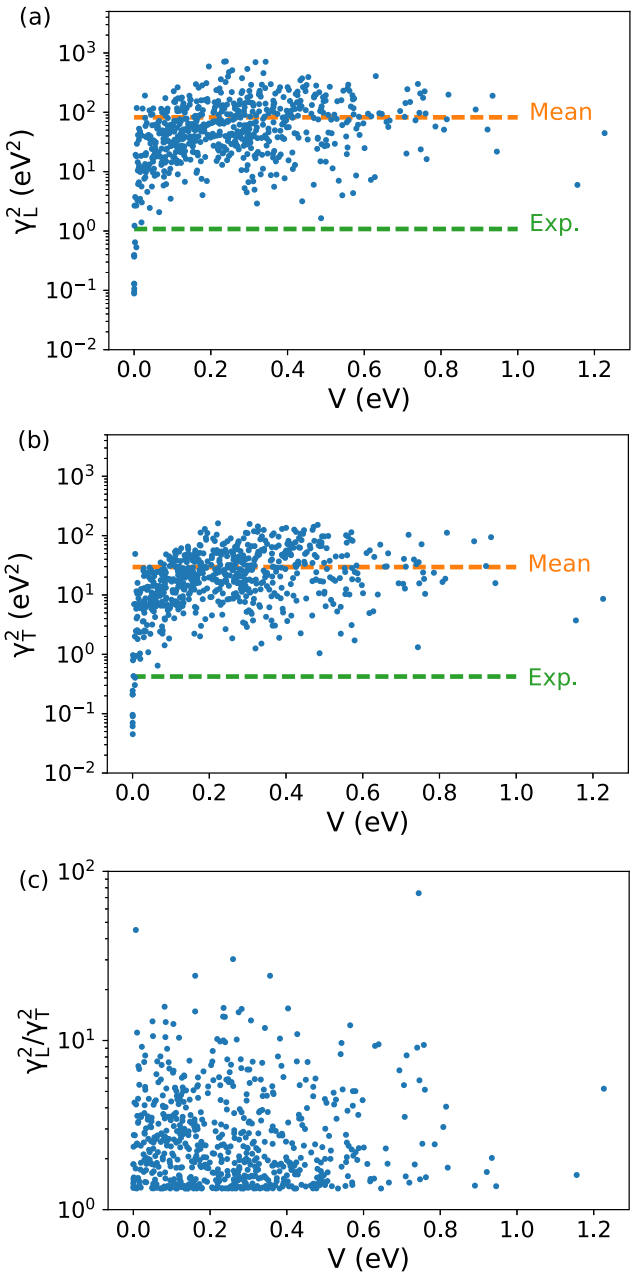

FIG. 3. (a) Longitudinal and (b) transverse deformation potentials as a function of V. The green dashed lines represent experimental values [50], while the orange lines are the numerical averages. In (c), we show the ratio γ_L^2/γ_T^2 for each TLS.

B. Classification of TLSs

Inspecting the atomic motions taking place in TLSs, we noticed that most TLSs can be sorted into one of three categories that will be referred to as types I–III. This classification remains empirical and some TLSs can share characteristics from more

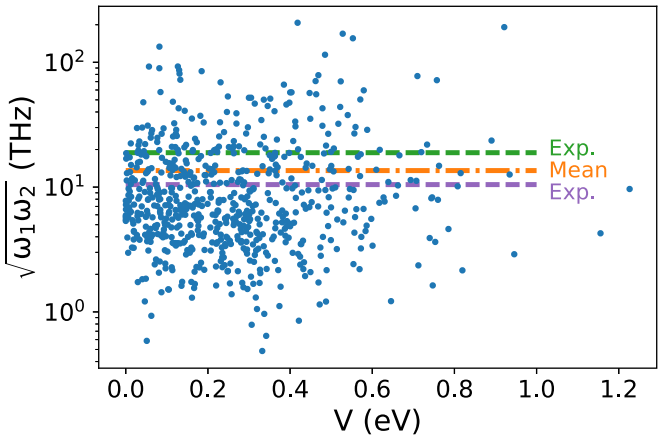

FIG. 4. Effective attempt frequency $\sqrt{\omega_1\omega_2}$ as a function of V. The orange dashed line represents the numerical average while the green and purple dashed lines are experimental values for SiO_2 deposited by IBS [21] and for bulk vitreous SiO_2 [24], respectively.

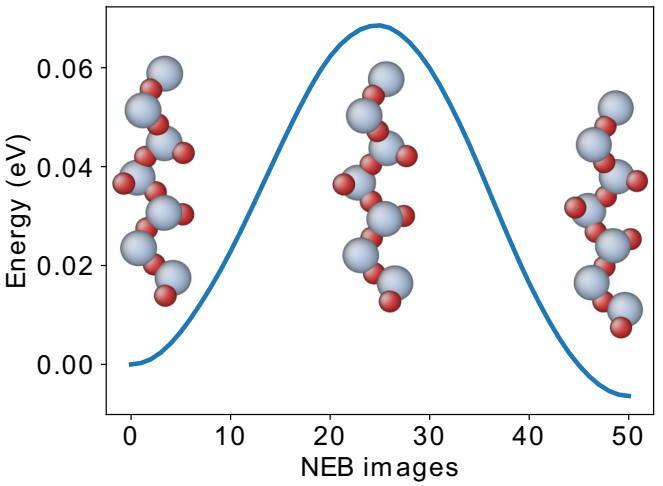

FIG. 6. Example of minimum energy path for a TLS of type II with snapshots of the initial, saddle, and final configurations. Only atoms with a displacement larger than 0.3 Å are shown.

than one type. We discuss in the following mostly archetypical cases.

1. Type I

In this type of TLS, an Si atom changes tetrahedron, as illustrated in Fig. 5. These transitions are highly localized and induce a significant displacement (i.e., larger than 0.3 Å) for less than a dozen atoms. During the transition, the Si atom breaks a SiO bond, leaves an O atom (noted *A* in the figure), and forms a new SiO bond with another O atom (noted *B*). Such transition is energetically possible only when either the *A* or *B* atom is ill-coordinated, with one or three Si neighbors, and the other O atom is well-coordinated, with two Si neighbors. The ill- and well-coordinated O atoms are then switched during the transition.

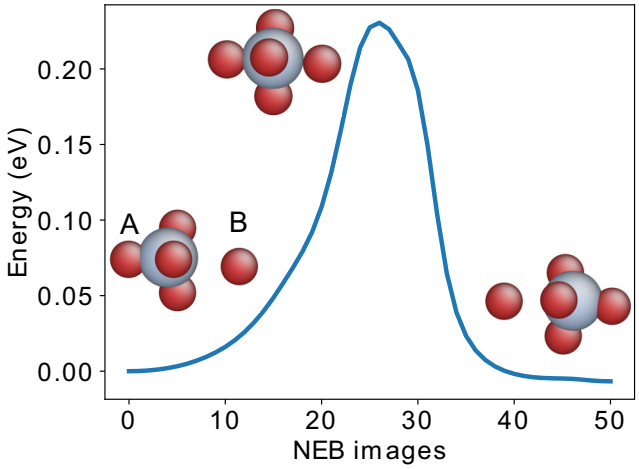

FIG. 5. Example of minimum energy path for a TLS of type I. The three snapshots show from left to right: the initial, saddle, and final configurations of the TLS. The oxygen and silicon atoms are shown in red and gray, respectively. Only atoms with a displacement larger than 0.3 Å are shown.

As illustrated in Fig. 5, the energy profile of type-I TLSs is often highly symmetrical, reflecting the structural symmetry between the initial and final configurations. The energy barrier is high (typically above 0.2 eV) because it involves breaking SiO bonds. Similar atomic motions have been observed in alumina by Paz *et al.* [52], where an Al atom can oscillate between two O neighbors.

2. Type II

This second category involves mainly the displacement of O atoms. An example is shown in Fig. 6, where several interconnected SiO_4 tetrahedra rotate, leading to the simultaneous and coordinated jump of O atoms from one side of their Si-O-Si bond to the other. The number of tetrahedra involved in these rotations varies from 3 to about 10. Such events have already been reported in atomic-scale studies of SiO_2 [26]. Type-II TLSs are highly delocalized and involve quasi-1D chains of Si-O-Si bonds and sometimes rings of Si-O-Si bonds. As all O atoms jump simultaneously, the energy profile shows a single energy barrier and since no SiO bond is broken, the energy barrier is rather low, typically less than 0.2 eV. The saddle occurs when the O atoms are compressed in the middle of their Si-O-Si bonds.

3. Type III

The third category encompassed events in which an O atom carries the largest displacement, going from being twofolded to threefolded (3 Si neighbors) or changing one of its Si neighbors (an Si atom ends up fivefolded). An illustration is shown in Fig. 7. Type-III TLSs are usually strongly asymmetrical because they create a coordination defect and the final state is highly metastable. We checked that applying a small strain to the simulation cell is often sufficient to make the final state unstable. Type-III transitions also require a high energy because they involve the breaking of SiO bonds.

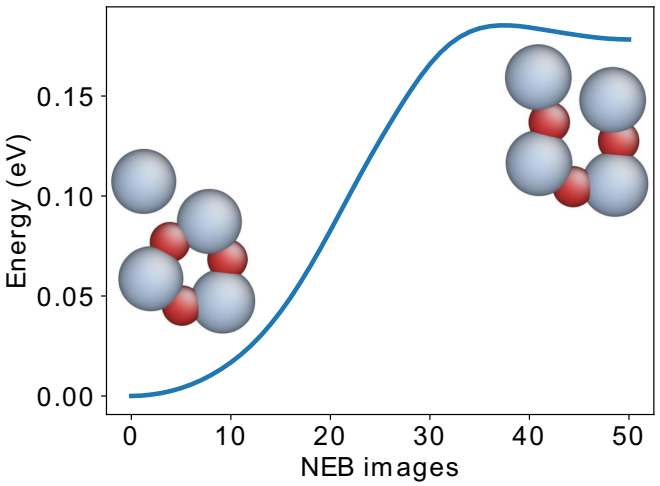

FIG. 7. Example of minimum energy path for a TLS of type III with snapshots of the initial and final configurations. Only atoms with a displacement larger than 0.3 Å are shown.

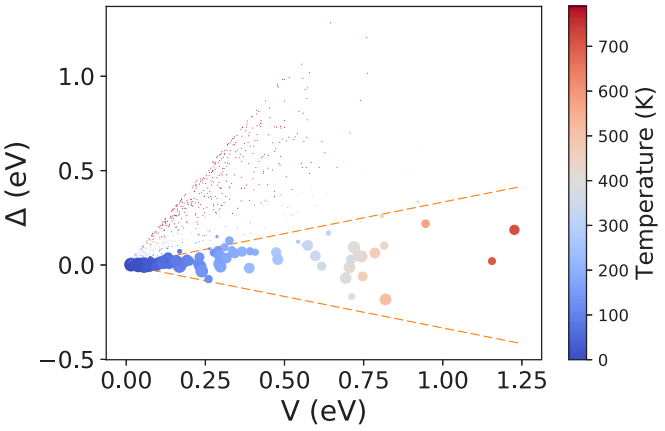

FIG. 9. Scatter plot of the TLS sampling showing each TLS with a symbol whose size scales logarithmically with the maximum dissipation produced by the TLS and a color which depends on the temperature at which this maximum dissipation is reached. Orange lines of expression $\Delta = \pm V/3$ were added to show empirically the region of high-dissipative TLSs.

IV. APPLICATION OF THE TLS MODEL

A. Full calculation

Figure 8 represents the dissipation computed from Eq. (1) for a longitudinal wave at 10 kHz. Transverse dissipation is qualitatively similar and will not be discussed here. In addition, dissipation was not computed below 10 K as quantum effects are not included in present study. To our knowledge, this is the first time the TLS model is applied on discrete TLSs without any approximation on their statistical distribution.

The numerical dissipation is compared in Fig. 8 to three sets of experimental data obtained on high-purity bulk fused silica in Refs. [16,19] and on 1-μm-thin films produced by IBS in Ref. [21]. It is important to note that compared to bulk vitreous silica, deposited thin films are known to be less relaxed and prone to structural defects, being sometimes even porous [53]. We also note that the experimental data were obtained

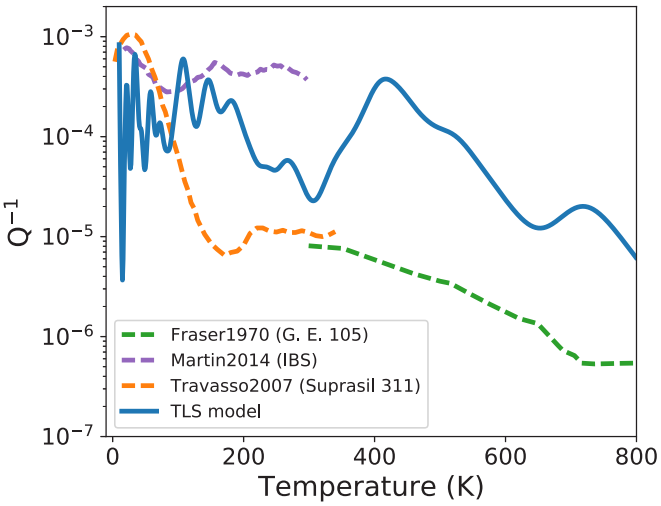

FIG. 8. Longitudinal dissipation at 10 kHz as a function of temperature, predicted using the numerical TLS sampling and compared to the experimental measurements of Refs. [16,19,21].

at different frequencies (1.5 MHz in Ref. [16], 3.8 kHz in Ref. [19], and 10 kHz in Ref. [21]), but these differences will be neglected here because the shape and magnitude of dissipation vary slowly with frequency.

We see in Fig. 8 that at low temperatures, below about 100 K, all data, numerical and experimental, are in qualitative agreement. At higher temperatures, the experimental dissipation in bulk silica decreases rapidly, while the numerical dissipation and that obtained in IBS thin films remain rather constant. The numerical dissipation then shows a high-temperature tail, which decreases slowly up to 800 K. Globally, the numerical dissipation is closer to IBS silica both in amplitude and shape. This was to be expected since the numerical glasses are quenched rapidly and contain coordination defects. Their structure is therefore closer to that of IBS silica than well-relaxed vitreous silica.

The numerical signal is made of peaks, which come from the contribution of individual TLSs. The present sampling is therefore not large enough to obtain a smooth prediction for dissipation. The reason is that only a very small fraction of the TLSs identified here contribute significantly to dissipation. To show this, we computed the maximum dissipation that each TLS (labelled ℓ) can produce, expressed from Eq. (1) as

$$q^{-1}_{\max,\ell} = \frac{\gamma_\ell^2}{\mathcal{V}C} \max_T \left(A_\ell \frac{\omega\tau_\ell}{1+\omega^2\tau_\ell^2} \right). \tag{7}$$

Figure 9 shows each TLS with a circle, whose size depends on $q^{-1}_{\max}$ and whose color depends on the temperature at which this maximum is reached. We had to use a logarithmic scale for the symbol size because of the enormous difference between low- and high-dissipative TLSs. We see clearly that only a very small fraction of TLSs contribute to dissipation. More quantitatively, only 41 TLSs in the 668 sample present a maximum above 10^{-5} and therefore produce a significant dissipation. We see in Fig. 9 that only TLSs with a small asymmetry, those near the $\Delta = 0$ line, contribute. We could not express analytically $q^{-1}_{\max,\ell}$ nor the corresponding optimum temperature $T_{\max,\ell}$ in the

general case. However, it can be shown that along the $\Delta = 0$ line, $T_{\max,\ell}$ increases almost linearly with V and that, at fixed V, $q^{-1}_{\max,\ell}$ is maximum for $\Delta = 0$. We checked numerically that $T_{\max,\ell}$ varies slowly near $\Delta = 0$ at fixed V. Thus, assuming a constant $T_{\max,\ell}$, it is straightforward to show that at fixed V, $q^{-1}_{\max,\ell}$ decreases exponentially with $|\Delta|/k_B T_{\max,\ell} \propto |\Delta|/V$. The dissipation is therefore maximum along the $\Delta = 0$ line and decreases exponentially away from it, with a characteristic energy proportional to V. This explains why in Fig. 9, only the TLSs in a cone around the $\Delta = 0$ line produce dissipation. Empirically, this cone has equation $|\Delta| < V/3$, as illustrated in Fig. 9.

Also, as said above, $T_{\max,\ell}$ increases linearly with V along the $\Delta = 0$ line, which is consistent with the intuitive result that TLSs of higher energy barriers are activated at higher temperatures. This is also visible in Fig. 9, where the temperature color varies from blue to red as V increases. Finally, we note in Fig. 8 that the numerical dissipation shows a gap around 350 K, which is also visible in Fig. 9 through the low density of contributing TLSs near 0.5 eV. At this point, we do not know if this is a physical effect or an artifact of the limited size of our sampling.

B. Approximations

Above, we have used the detailed characteristics of each TLS to predict dissipation. However, in applications of the TLS model, approximations on the TLS statistics are usually applied without clear justification. We have already seen in Sec. III A 2 that contrary to the usual assumption, asymmetries and energy barriers are not independent for the simple reason that $\Delta < 2V$ [28]. In this section, we wish to evaluate the impact of three other typical approximations, related to the TLS attempt frequency, deformation potential and energy asymmetry.

1. Attempt frequency

When applying the TLS model, both experimentally and numerically, the attempt frequencies in the initial and final states $\omega_{1/2}$ are usually assumed identical and equal to a mean value common to all TLSs. To test this approximation, Fig. 10 compares the dissipations obtained using the full sample (in blue), or assuming that for each TLS $\omega_1 = \omega_2 \equiv \sqrt{\omega_1\omega_2}$ (in orange) and finally, using for each TLS the average effective attempt frequency of the sample, $\langle\sqrt{\omega_1\omega_2}\rangle = 13.6$ THz, shown in Fig. 4. We see that these approximations do not affect the overall amplitude of the dissipation below 200 K, but only its details and they shorten the high-temperature tail above 400 K, particularly when an average attempt frequency is used. Attempt frequencies therefore play a limited role, particularly at low temperatures, even if they vary by 2 orders of magnitude among TLSs, as seen in Fig. 4. The reason is that the attempt frequencies appear in Eq. (3) as pre-exponential factors and have a limited influence on the relaxation time and the dissipation.

2. Deformation potential

Another typical assumption used to treat both experimental [23,31,54] and numerical [27,28] data is to assume that all TLSs have the same deformation potential. To test this approximation, we compare in Fig. 11 the full calculation (in blue) with the dissipation computed when all TLSs have the same deformation potential equal to the mean value of the sampling, $\langle\gamma_L^2\rangle = 82.3$ eV^2, shown in Fig. 3(a). We see that again, even if the deformation potential varies by about two orders of magnitude among TLSs and scales linearly with the TLS contribution in Eq. (1), using a single reference deformation potential for all TLSs affects the dissipation even less than the attempt frequencies.

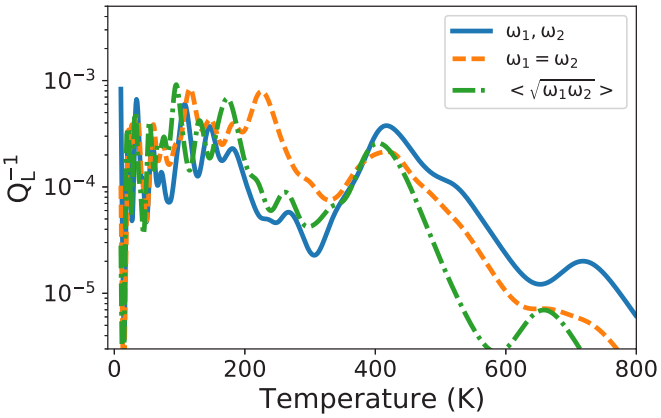

FIG. 10. Longitudinal dissipation at 10 kHz predicted using the full sample, i.e., individual attempt frequencies, ω_1 and ω_2, for each TLS (blue curve), or assuming that $\omega_1 = \omega_2 \equiv \sqrt{\omega_1\omega_2}$ (orange curve), or using for every TLS the mean effective frequency $\langle\sqrt{\omega_1\omega_2}\rangle = 13.6$ THz, computed over the entire sample (green curve).

3. Asymmetry

A third typical assumption is to ignore TLSs with large asymmetries, which is justified from our above discussion. However, the rule to discard TLSs should be chosen with care. For instance, a selection rule was introduced in Refs. [27,33], consisting in ignoring all TLSs with asymmetries higher than 0.1 eV. This approximation is tested in Fig. 12 and reproduces perfectly the full calculation below 300 K, but cuts-off the high-temperature tail above 400 K. This result is expected

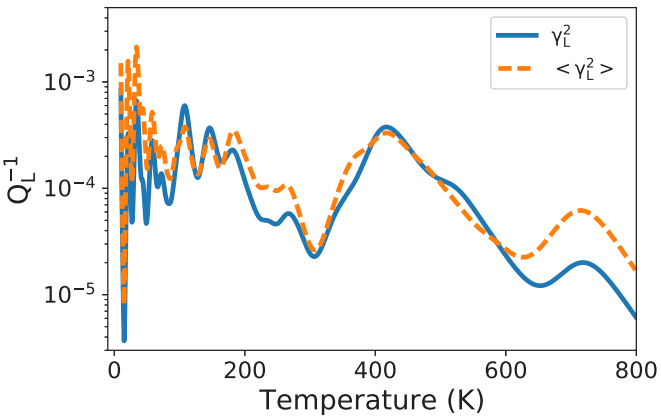

FIG. 11. Longitudinal dissipation at 10 kHz predicted using the full sample, i.e., individual deformation potentials for each TLS (blue curve), or using for every TLS the mean deformation potential ($\langle\gamma_L^2\rangle = 82.3$ eV^2), computed over the entire sample.

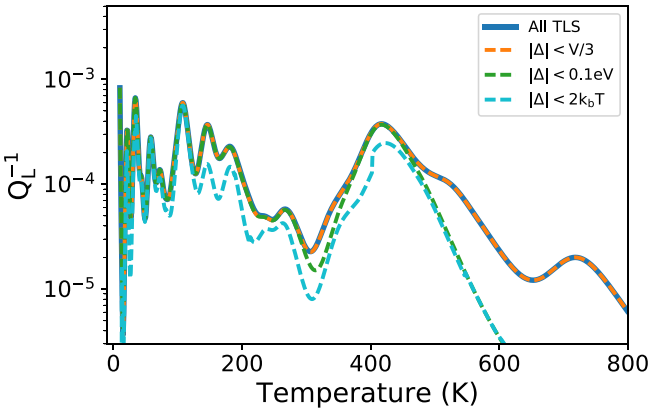

FIG. 12. Longitudinal dissipation at 10 kHz predicted using the full sample, i.e., individual asymmetries (blue curve), or keeping only the TLSs such that $|\Delta| < V/3$ (orange curve), or keeping TLSs such that $\Delta < 0.1$ eV.

from Fig. 9, where TLSs that contribute at low temperatures have indeed asymmetries within ± 0.1 eV. However, at higher temperatures and energy barriers, the range of asymmetries increases and the approximation artificially removes important barriers. Similarly, the approximation used in Ref. [24], where TLSs with $|\Delta| > 2k_BT$ were neglected, also cuts-off the high-temperature tail of the dissipation. A better empirical approximation is to ignore TLSs with an asymmetry larger than $V/3$ (i.e., TLSs outside the cone identified in Fig. 9), which, as seen in Fig. 12, predicts dissipation in perfect agreement with the full calculation, even at high temperatures.

V. DISCUSSION AND CONCLUSION

We have shown here that using an atomic-scale model of amorphous silica in conjunction with the TLS model allows to predict internal friction in qualitative agreement with experiments, without requiring any approximation to simplify the statistical properties of the TLSs. The dissipation predicted numerically is closer to that of poorly relaxed thin films, as expected from the fact that the numerical glasses are quenched on MD time scales and therefore extremely rapidly compared to vitreous silica. As a result, the numerical glasses still contain structural defects in the form of coordination defects (see Table I), which strongly affect dissipation at elevated temperatures. Comparison with the experiments is, however, limited by several factors. Impurities are known to strongly impact dissipation and cannot be fully controlled experimentally [16]. Also the comparison between numerical and experimental TLS distributions [27,28] is difficult because the experiments were analyzed assuming that the energy barriers and asymmetries are independent, an assumption, which is not supported by the present results. On the numerical side, we have used the simplest interatomic potential to model amorphous silica and there is no guarantee that this potential represents properly low-activation barriers. More advanced potentials, which account for charge polarization [55,56], should be tested. Also, we considered larger samples than in previous studies [26–28,33], but they may still be too small to fully account for the collective rotations of type-II TLSs. Considering larger systems remains, however, computationally challenging. Several TLSs may appear simultaneously in larger systems during the MD searches since the latter are performed at elevated temperature, which would clearly complicate the analysis.

The present work shows the importance of sampling low-energy barriers, typically <0.5 eV, which control dissipation up to room temperature, the range of interest for many applications. Finding low-activation energies remains a challenge. In particular, eigenvector-following methods, such as the activation-relaxation technique (ART) [57], tend to identify high energy barriers, typically up to 10 eV in SiO_2 [36]. Using MD at high temperatures offers a practical solution but remains numerically inefficient. In the present case, we ran 115 000 searches to identify less than 1000 independent TLSs. However, we should note that the real numerical bottleneck in the present calculations is the initial quench to produce well-relaxed glasses. Progress has been achieved recently [58], but it remains to be seen whether this new approach can be extended to realistic glasses like silica.

By analyzing the atomic motions involved in TLSs, we defined three types of transitions, which contribute differently to dissipation. We have seen that type-III TLSs produce coordination defects and involve large asymmetries. They are found in Fig. 9 near the $\Delta = 2V$ line and therefore do not participate in the dissipation. They unfortunately represent the largest fraction of TLSs found here and are one reason why the present sampling is too small to predict a smooth dissipation curve. The two other types of TLSs are more symmetrical and are found near the $\Delta = 0$ line of high dissipation. Type-I TLSs are centered on coordination defects in the initial configuration and have large energy barriers, typically, above 0.2 eV, because they involve breaking SiO bonds. From Fig. 9, we understand that these TLSs contribute to dissipation above 300 K and are responsible for the high-temperature tail of dissipation in Fig. 8. Since these TLSs are centered on coordination defects, we expect that they do not exist in slowly-relaxed bulk vitreous silica, which explains why dissipation decreases rapidly at high temperatures in this case. Finally, type-II TLSs involve the cooperative rotation of SiO-Si bonds and have low-energy barriers because they do not require breaking SiO bonds. We therefore understand from Fig. 9 that type-II TLSs contribute below 300 K and are responsible for the low-temperature portion of the dissipation curve where both numerical and experimental data agree at least qualitatively. Since type-II TLSs have very low activation energies, they are probably also involved in dissipation in the quantum regime, as proposed by Reinisch and Heuer [26]. Finally, we wish to note that the example in Fig. 6 can be considered as a canonical TLS, since its activation barrier (∼65 meV) and asymmetry ($|\Delta| \sim V/10$) closely match the characteristic energies estimated from experimental data by Vacher *et al.* [24]. Interestingly, the collective motion of SiO-Si bonds is also responsible for energy dissipation at high frequency in the THz regime, although in this case, dissipation arises from the harmonic bending motion of these bonds around the equilibrium configuration [43].

The classification proposed here remains empirical. It would be interesting to develop a mathematical criterion in order to sort automatically TLSs. Also, it remains to be seen whether this classification can be adapted to more complex

glasses compared to the almost perfect arrangement of amorphous silica.

Finally, we have tested several classical approximations. Using an average attempt frequency is justified, if one is interested in low-temperature dissipation. Replacing the deformation potential by its average has a smaller effect, which is quite unexpected since the dissipation due to a TLS directly scales with its deformation potential. Also, we note that we found numerical values about 100 times larger than reported previously, both experimentally [50] and numerically [27,28]. We believe that the discrepancy with the experiments is because the latter were performed in the quantum regime. Concerning numerical works, the reason might be a size effect, but this point should be explored in more details. Since the deformation potential and attempt frequency can be replaced by their averages, the contribution of a TLS is only a function of its asymmetry Δ and its energy barrier V. We have seen that these variables cannot be assumed statistically independent. However, the present sampling is not large enough to estimate whether a simplified coupled distribution, $P(\Delta, V)$, exists.

In Appendixes A–C, we detail the theory leading to the expression of dissipation 1. We follow an approach similar to that of Jäckle *et al.* [12], but fully account for the tensorial nature of the strains and stresses and for the possible difference between the attempt frequencies in both states of the TLSs.

ACKNOWLEDGMENTS

The authors acknowledge support from LABEX iMUST (ANR-10-LABX-0064) of Université de Lyon (program "Investissements d'Avenir," ANR-11-IDEX-0007).

APPENDIX A: COMPLEX MODULUS

1. Equilibrium probabilities and detailed balance

We consider a TLS with 2 metastable states, noted 1 and 2, linked by a double-well potential, $V(x)$ as shown in Fig. 1 of the main text. We note p_1 and p_2, the probabilities to find the TLS in either state 1 or 2, which denote the basins on either sides of the energy barrier. $\bar{p}_1$ and $\bar{p}_2$ are the equilibrium probabilities.

At equilibrium, the probability to be at position x is proportional to $\exp(-V(x)/k_bT)$. Therefore

$$\bar{p}_1 \propto \int_1 \exp(-\beta V(x))dx \tag{A1}$$

and

$$\bar{p}_2 \propto \int_2 \exp(-\beta V(x))dx, \tag{A2}$$

where the integrals are performed over the basins of both states and $\beta = 1/k_bT$. Using a harmonic approximation, with ω_1^2 and ω_2^2 the curvatures at the bottom of both states, we have

$$\bar{p}_1 = \frac{1}{1+\exp(-\beta\Delta)\frac{\omega_1}{\omega_2}},$$
$$\bar{p}_2 = \frac{1}{1+\exp(\beta\Delta)\frac{\omega_2}{\omega_1}}, \tag{A3}$$

where Δ is the energy asymmetry between states 1 and 2, as in the main text.

According to the harmonic transition state theory [34], the transition rates between states 1 and 2 are

$$a_{12} = \frac{\omega_1}{2\pi}\exp(-\beta E_a),$$
$$a_{21} = \frac{\omega_2}{2\pi}\exp\left(-\beta(E_a-\Delta)\right), \tag{A4}$$

where E_a is the energy barrier from state 1 to 2. One can easily check that Eqs. (A3) and (A4) satisfy the detailed balance, i.e., $\bar{p}_1 a_{12} = \bar{p}_2 a_{21}$.

2. Deformation potential

The TLS is in a volume $\mathcal{V}$ subjected to a periodic applied strain tensor, $\bar{\bar{\epsilon}}(t)$. Dissipation occurs if the energy asymmetry, Δ, depends on the applied strain. Within an eigenstrain approach [35], such coupling occurs if an eigenstrain $\bar{\bar{\epsilon}}^\star$ is generated when the TLS transforms from state 1 to state 2. The energy asymmetry and stress then depend on the applied strain as (with repeated index summation)

$$\Delta(\bar{\bar{\epsilon}}) = \Delta + \frac{\mathcal{V}}{2}C^\infty_{ijkl}\left(\epsilon_{ij} - \frac{\upsilon_a}{\mathcal{V}}\epsilon^\star_{ij}\right)\left(\epsilon_{kl} - \frac{\upsilon_a}{\mathcal{V}}\epsilon^\star_{kl}\right),$$
$$\sigma_{ij} = C^\infty_{ijkl}\left(\epsilon_{kl} - \frac{\upsilon_a}{\mathcal{V}}\epsilon^\star_{kl}\right), \tag{A5}$$

where C^∞ is the tensor of elastic constants (including both affine and nonaffine contributions, since the latter relax over time scales much shorter than considered here [43]) and υ_a, the TLS volume. Introducing the deformation potential tensor

$$\gamma_{ij} = \left.\frac{\partial\Delta}{\partial\epsilon_{ij}}\right|_{\bar{\bar{\epsilon}}=0} = -\upsilon_a C^\infty_{ijkl}\epsilon^\star_{kl}, \tag{A6}$$

we have

$$\sigma_{ij} = C^\infty_{ijkl}\epsilon_{kl} + \frac{\gamma_{ij}}{\mathcal{V}}. \tag{A7}$$

If we introduce $\delta p_2(t) = p_2(t) - \bar{p}_2(0)$, the difference between the current probability of being in state 2, $p_2(t)$, and its equilibrium value in absence of applied strain, $\bar{p}_2(0)$, the time-dependent part of the stress is expressed as

$$\sigma_{ij} = C^\infty_{ijkl}\epsilon_{kl}(t) + \frac{\gamma_{ij}}{V}\delta p_2(t). \tag{A8}$$

Concerning the energy asymmetry, keeping only the first-order time-dependent term in Eq. (A5), we have

$$\Delta(\bar{\bar{\epsilon}}) = \Delta + \gamma_{ij}\epsilon_{ij}. \tag{A9}$$

We also note that, from Eq. (A7), the deformation potential can be calculated from the difference of internal stress in states 1 and 2 subjected to the same applied strain:

$$\gamma_{ij} = \mathcal{V}\Delta\sigma_{ij}. \tag{A10}$$

3. Master equation

Dissipation arises because the strain changes Δ [Eq. (A9)], which in turn changes the equilibrium probabilities, $\bar{p}_1$ and $\bar{p}_2$ [Eq. (A3)], and brings the system in an out-of-equilibrium state with a finite relaxation time. Following Ref. [12], the probabilities p_1 and p_2 are written in terms of master equations:

$$\dot{p}_1 = -p_1 a_{12} + p_2 a_{21},$$
$$\dot{p}_2 = p_1 a_{12} - p_2 a_{21}, \tag{A11}$$

where the transition rates, a_{12} and a_{21}, depend on time because of their dependence on Δ [Eq. (A4)]. Since $p_1 + p_2 = 1$, we have

$$\dot{p}_2 = -p_2(a_{12} + a_{21}) + a_{12}. \tag{A12}$$

We can define a time-dependent equilibrium:

$$\bar{p}_2(t) = \frac{a_{12}(t)}{a_{12}(t) + a_{21}(t)}. \tag{A13}$$

Inserting Eq. (A13) into Eq. (A12), we obtain

$$\dot{p}_2 = -(p_2 - \bar{p}_2(t))(a_{12}(t) + a_{21}(t)). \tag{A14}$$

We see from this equation and Eq. (A4) that to first order, the time dependence of the transition rates can be neglected, allowing to define a relaxation time, $\tau^{-1} = a_{12}(0) + a_{21}(0)$. Using $V = E_a - \Delta/2$, the relaxation time is rewritten as

$$\tau^{-1} = \frac{\sqrt{\omega_1\omega_2}}{\pi} \exp(-\beta V)\mathrm{ch}\left(\frac{\beta\Delta}{2} + \frac{1}{2}\ln\frac{\omega_2}{\omega_1}\right). \tag{A15}$$

From Eq. (A14) using $\delta p_2 = p_2 - \bar{p}_2(0)$, we have

$$\tau\dot{\delta}p_2 = -\delta p_2 + \bar{p}_2(t) - \bar{p}_2(0) \tag{A16}$$

From the definition of the coupling parameter, we have

$$\begin{aligned}\bar{p}_2(t) - \bar{p}_2(0) &= \bar{p}_2(\Delta + \gamma_{ij}\epsilon_{ij}(t)) - \bar{p}_2(\Delta) \\ &\simeq \frac{\partial\bar{p}_2}{\partial\Delta}\gamma_{ij}\epsilon_{ij}(t)\end{aligned} \tag{A17}$$

and from Eq. (A3):

$$\frac{\partial\bar{p}_2}{\partial\Delta} = -\frac{1}{4kT\mathrm{ch}^2\left(\frac{\beta\Delta}{2} + \frac{1}{2}\ln\frac{\omega_2}{\omega_1}\right)} \equiv -A. \tag{A18}$$

Finally, inserting Eq. (A17) with the definition of A into Eq. (A16), we obtain the following first-order differential equation for δp_2:

$$\tau\dot{\delta}p_2 = -\delta p_2 - A\gamma_{ij}\epsilon_{ij}, \tag{A19}$$

which is solved in the spectral domain, with $\epsilon \propto \exp(i\omega t)$:

$$\delta p_2 = -\frac{A}{1 + i\omega\tau}\gamma_{ij}\epsilon_{ij}. \tag{A20}$$

4. Complex modulus

From Eqs. (A8) and (A20), the tensor of complex elastic moduli is expressed as

$$C(\omega) = C^\infty - \frac{1}{\mathcal{V}}\frac{A}{1 + i\omega\tau}\bar{\bar{\gamma}} \otimes \bar{\bar{\gamma}}, \tag{A21}$$

with $\gamma \otimes \gamma$, the tensor of components $\gamma_{ij}\gamma_{kl}$. If the volume $\mathcal{V}$ contains a population of independent TLSs, with different $\bar{\bar{\gamma}}_\ell$, A_ℓ, and τ_ℓ, we obtain from the superposition principle:

$$C(\omega) = C^\infty - \frac{1}{\mathcal{V}}\sum_{\ell,\mathrm{TLS}}\frac{A_\ell}{1 + i\omega\tau_\ell}\bar{\bar{\gamma}}_\ell \otimes \bar{\bar{\gamma}}_\ell. \tag{A22}$$

APPENDIX B: LONGITUDINAL DISSIPATION

If the medium is deformed by a longitudinal wave along a unit vector $\vec{U}$, the corresponding strain tensor is $\epsilon(t)\vec{U} \otimes \vec{U}$, with elements $\epsilon(t)U_iU_j$. Dissipation is then given by the time delay between $\epsilon(t)$ and the tensile stress $\sigma = U_i\sigma_{ij}U_j$ along $\vec{U}$.

Glasses being isotropic, the static term in Eq. (A22) corresponding to C^∞ yields $\sigma = M\epsilon$, where $M = \lambda + 2\mu$ is the longitudinal modulus and λ and μ are the Lamé coefficients. The second term in Eq. (A22) yields for each TLS a coupling term of the form $\sum_{ijkl}\gamma_{ij}\gamma_{kl}U_iU_jU_kU_l = (\sum_{ij}\gamma_{ij}U_iU_j)^2$. Since a TLS can take any orientation with respect to the applied strain, we have to average this term over all strain directions:

$$\gamma_L^2 = \sum_{ijkl}\gamma_{ij}\gamma_{kl}\langle U_iU_jU_kU_l\rangle. \tag{B1}$$

Only even-power averages are nonzero and because of isotropy, there are only two distinct terms, $\langle U_X^4\rangle = \langle U_Y^4\rangle = \langle U_Z^4\rangle = 1/5$ and $\langle U_X^2U_Y^2\rangle = \langle U_X^2U_Z^2\rangle = \langle U_Y^2U_Z^2\rangle = 1/15$. Thus

$$\begin{aligned}\gamma_L^2 = {}& \tfrac{1}{5}\left(\gamma_{XX}^2 + \gamma_{YY}^2 + \gamma_{ZZ}^2\right) \\ &+ \tfrac{2}{15}(\gamma_{XX}\gamma_{YY} + \gamma_{XX}\gamma_{ZZ} + \gamma_{YY}\gamma_{ZZ}) \\ &+ \tfrac{4}{15}\left(\gamma_{XY}^2 + \gamma_{XZ}^2 + \gamma_{YZ}^2\right).\end{aligned} \tag{B2}$$

This orientation-average is unchanged under a rotation of the deformation potential tensor, and can be expressed in terms of the invariants, $I_1 = \mathrm{tr}(\bar{\bar{\gamma}})$ and $I_2 = \mathrm{tr}(\bar{\bar{\gamma}}^2)$:

$$\gamma_L^2 = \tfrac{1}{15}\left(2I_2 + I_1^2\right). \tag{B3}$$

The frequency-dependent longitudinal modulus is therefore expressed as

$$M(\omega) = M - \frac{1}{\mathcal{V}}\sum_{\ell,\mathrm{TLS}}\frac{A_\ell}{1 + i\omega\tau_\ell}\gamma_{L,\ell}^2 \tag{B4}$$

and the dissipation is given by the ratio of the imaginary and real parts of the complex modulus:

$$Q_L^{-1}(\omega) = \frac{\sum_\ell A_\ell\frac{\omega\tau_\ell}{1+\omega^2\tau_\ell^2}\gamma_{L,\ell}^2}{\mathcal{V}M - \sum_\ell\frac{A_\ell}{1+\omega^2\tau_\ell^2}\gamma_{L,\ell}^2}. \tag{B5}$$

We have checked that for the present system, systematically, $\sum_\ell A_\ell\langle\gamma_\ell^2\rangle_L \ll \mathcal{V}M$, such that

$$Q_L^{-1}(\omega) \simeq \frac{1}{\mathcal{V}M}\sum_{\ell,\mathrm{TLS}}A_\ell\frac{\omega\tau_\ell}{1 + \omega^2\tau_\ell^2}\gamma_{L,\ell}^2. \tag{B6}$$

APPENDIX C: TRANSVERSE DISSIPATION

With a transverse wave, the medium is sheared along a unit vector $\vec{U}$ parallel to a plane of normal $\vec{V}$. The corresponding strain tensor is $\epsilon(t)(U \otimes V + V \otimes U)/2$. The time-independent term in Eq. (A22) now yields a shear stress $\sigma = G\epsilon$, where G is the shear modulus and the average coupling term is

$$\gamma_T^2 = \sum_{ijkl}\gamma_{ij}\gamma_{kl}\langle U_iV_jU_kV_l\rangle. \tag{C1}$$

Again, only even-power averages are nonzero, and accounting for the fact that $\vec{U}$ and $\vec{V}$ are perpendicular, we find $\langle U_X^2V_X^2\rangle = \langle U_Y^2V_Y^2\rangle = \langle U_Z^2V_Z^2\rangle = 1/15$, $\langle U_XV_XU_YV_Y\rangle = \langle U_YV_YU_ZV_Z\rangle = \langle U_ZV_ZU_XV_X\rangle = -1/15$, and $\langle U_X^2V_Y^2\rangle = \langle U_X^2V_Z^2\rangle = \langle U_Y^2V_Z^2\rangle = 3/15$. Therefore

$$\begin{aligned}\gamma_T^2 = {}& \tfrac{1}{15}\left(\gamma_{XX}^2 + \gamma_{YY}^2 + \gamma_{ZZ}^2\right) \\ &- \tfrac{1}{15}(\gamma_{XX}\gamma_{YY} + \gamma_{YY}\gamma_{ZZ} + \gamma_{ZZ}\gamma_{XX}) \\ &+ \tfrac{3}{15}\left(\gamma_{XY}^2 + \gamma_{XZ}^2 + \gamma_{YZ}^2\right),\end{aligned} \tag{C2}$$

which is expressed in terms of tensor invariants as

$$\gamma_T^2 = \tfrac{1}{15}\left(\tfrac{3}{2}I_2 - \tfrac{1}{2}I_1^2\right). \tag{C3}$$

The resulting dissipation is

$$Q_T^{-1}(\omega) \simeq \frac{1}{\mathcal{V}G}\sum_{\ell,\mathrm{TLS}} A_\ell \frac{\omega\tau_\ell}{1+\omega^2\tau_\ell^2}\gamma_{T,\ell}^2. \tag{C4}$$

[1] R. Lifshitz and M. L. Roukes, Phys. Rev. B **61**, 5600 (2000).
[2] B. H. Houston, D. M. Photiadis, M. H. Marcus, J. A. Bucaro, X. Liu, and J. F. Vignola, Appl. Phys. Lett. **80**, 1300 (2002).
[3] M. Li, H. X. Tang, and M. L. Roukes, Nat. Nanotechnol. **2**, 114 (2007).
[4] P. R. Saulson, Phys. Rev. D **42**, 2437 (1990).
[5] R. Flaminio, J. Franc, C. Michel, N. Morgado, L. Pinard, and B. Sassolas, Class. Quant. Grav. **27**, 084030 (2010).
[6] M. Granata *et al.*, Opt. Lett. **38**, 5268 (2013).
[7] J. L. Snoeck, Physica **8**, 711 (1941).
[8] P. G. Bordoni, J. Acoust. Soc. Am. **26**, 495 (1954).
[9] W. A. Phillips, J. Low Temp. Phys. **7**, 351 (1972).
[10] P. W. Anderson, B. Halperin, and C. M. Varma, Philos. Mag. **25**, 1 (1972).
[11] J. Jäckle, Z. Phys. **257**, 212 (1972).
[12] J. Jäckle, L. Piché, W. Arnold, and S. Hunklinger, J. Non-Cryst. Solids **20**, 365 (1976).
[13] W. A. Phillips, Rep. Prog. Phys. **50**, 1657 (1987).
[14] K. S. Gilroy and W. A. Phillips, Philos. Mag. B **43**, 735 (1981).
[15] M. E. Fine, H. Van Duyne, and N. T. Kenney, J. Appl. Phys. **25**, 402 (1954).
[16] D. B. Fraser, J. Appl. Phys. **41**, 6 (1970).
[17] D. G. Cahill and J. E. Van Cleve, Rev. Sci. Instr. **60**, 2706 (1989).
[18] R. Keil, G. Kasper, and S. Hunklinger, J. Non-Cryst. Solids **164**, 1183 (1993).
[19] F. Travasso, P. Amico, L. Bosi, F. Cottone, A. Dari, L. Gammaitoni, H. Vocca, and F. Marchesoni, Europhys. Lett. **80**, 50008 (2007).
[20] D. R. Queen, X. Liu, J. Karel, H. C. Jacks, T. H. Metcalf, and F. Hellman, J. Non-Cryst. Solids **426**, 19 (2015).
[21] I. W. Martin, R. Nawrodt, K. Craig, C. Schwarz, R. Bassiri, G. Harry, J. Hough, S. Penn, S. Reid, R. Robie *et al.*, Class. Quant. Grav. **31**, 035019 (2014).
[22] S. Hunklinger, W. Arnold, St. Stein, R. Nava, and K. Dransfeld, Phys. Lett. A **42**, 253 (1972).
[23] D. Tielbürger, R. Merz, R. Ehrenfels, and S. Hunklinger, Phys. Rev. B **45**, 2750 (1992).
[24] R. Vacher, E. Courtens, and M. Foret, Phys. Rev. B **72**, 214205 (2005).
[25] C. Levelut, R. Le Parc, and J. Pelous, Phys. Rev. B **73**, 052202 (2006).
[26] J. Reinisch and A. Heuer, Phys. Rev. Lett. **95**, 155502 (2005).
[27] R. Hamdan, J. P. Trinastic, and H. P. Cheng, J. Chem. Phys. **141**, 054501 (2014).
[28] C. R. Billman, J. P. Trinastic, D. J. Davis, R. Hamdan, and H.-P. Cheng, Phys. Rev. B **95**, 014109 (2017).
[29] J. F. Berret and M. Meissner, Z. Phys. B **70**, 65 (1988).
[30] J. Wiedersich, S. V. Adichtchev, and E. Rössler, Phys. Rev. Lett. **84**, 2718 (2000).
[31] U. Buchenau, Phys. Rev. B **63**, 104203 (2001).
[32] A. Heuer and R. J. Silbey, Phys. Rev. Lett. **70**, 3911 (1993).
[33] J. P. Trinastic, R. Hamdan, C. Billman, and H.-P. Cheng, Phys. Rev. B **93**, 014105 (2016).
[34] G. H. Vineyard, J. Phys. Chem. Solids **3**, 121 (1957).
[35] T. Mura, *Micromechanics of Defects in Solids* (Springer, Dordrecht, 1982).
[36] P. Koziatek, J.-L. Barrat, and D. Rodney, J. Non-Cryst. Solids **414**, 7 (2015).
[37] B. W. H. van Beest, G. J. Kramer, and R. A. van Santen, Phys. Rev. Lett. **64**, 1955 (1990).
[38] S. N. Taraskin and S. R. Elliott, Phys. Rev. B **56**, 8605 (1997).
[39] M. S. Shell, P. G. Debenedetti, and A. Z. Panagiotopoulos, Phys. Rev. E **66**, 011202 (2002).
[40] B. Mantisi, A. Tanguy, G. Kermouche, and E. Barthel, Eur. Phys. J. B **85**, 304 (2012).
[41] N. S. Shcheblanov, B. Mantisi, P. Umari, and A. Tanguy, J. Non-Cryst. Solids **428**, 6 (2015).
[42] A. Carré, L. Berthier, J. Horbach, S. Ispas, and W. Kob, J. Chem. Phys. **127**, 114512 (2007).
[43] T. Damart, A. Tanguy, and D. Rodney, Phys. Rev. B **95**, 054203 (2017).
[44] A. Rahmani, M. Benoit, and C. Benoit, Phys. Rev. B **68**, 184202 (2003).
[45] S. Le Roux and P. Jund, Comput. Mater. Sci. **49**, 70 (2010).
[46] G. Mills and H. Jónsson, Phys. Rev. Lett. **72**, 1124 (1994).
[47] G. Mills, H. Jónsson, and G. K. Schenter, Surf. Sci. **324**, 305 (1995).
[48] G. Henkelman, B. P. Uberuaga, and H. Jónsson, J. Chem. Phys. **113**, 9901 (2000).
[49] W. Gööze and L. Sjögren, Rep. Prog. Phys. **55**, 241 (1992).
[50] P. Doussineau, M. Matecki, and W. Schön, J. Phys. (France) **44**, 101 (1983).
[51] A. Heuer, Phy. Rev. B **56**, 161 (1997).
[52] A. P. Paz, I. V. Lebedeva, I. V. Tokatly, and A. Rubio, Phys. Rev. B **90**, 224202 (2014).
[53] S. Gelin, Ph.D. thesis, Université Paris-Est, 2016.
[54] K. A. Topp and D. G. Cahill, Z. Phys. B **101**, 235 (1996).
[55] J. R. Kermode, S. Cereda, P. Tangney, and A. De Vita, J. Chem. Phys. **133**, 094102 (2010).
[56] P. Brommer, P. Beck, A. Chatzopoulos, F. Gähler, J. Roth, and H. R. Trebin, J. Chem. Phys. **132**, 194109 (2010).
[57] N. Mousseau and G. T. Barkema, Phys. Rev. E **57**, 2419 (1998).
[58] A. Ninarello, L. Berthier, and D. Coslovich, Phys. Rev. X **7**, 021039 (2017).